RSC Advances

ROYAL SOCIETY OF CHEMISTRY

www.rsc.org/advances

RSC Advances

ARTICLE

Fabrication of magnetic bimetallic Fe_3O_4@Au-Pd hybrid nanoparticles with recyclable and efficient catalytic properties

Received 00th January 20xx,
Accepted 00th January 20xx

DOI: 10.1039/x0xx00000x

www.rsc.org/

Qingdong Xia, Shanshan Fu, Guojuan Ren, Fang Chai*, Jingjie Jiang*, Fengyu Qu*

Bimetallic nanostructures show exciting potential as materials for effective catalysis. Magnetically recoverable bimetallic nanoparticles are promising catalysts for chemical reactions. Here, Fe_3O_4@Pd and Fe_3O_4@Au-Pd hybrid nanoparticles were synthesized and used as catalysts. The morphology, composition, and structure of Fe_3O_4@Pd and Fe_3O_4@Au-Pd hybrid nanoparticles were fully characterized by scanning and transmission electron microscopy, energy dispersive spectroscopy, high angle annular dark-field scanning TEM, X-ray powder diffraction, X-ray photoelectron spectroscopy techniques, etc. The Fe_3O_4@Pd and Fe_3O_4@Au-Pd nanoparticles have shown excellent catalytic activity towards the reduction of nitrophenols and potassium hexacyanoferrate (III). In addition, the magnetic bimetallic heterogeneous nanoparticles can be easily recycled show good reusability as a conversion higher than 99% was achieved after 6 cycles.

Introduction

Bimetallic nanoparticles consist of two metals and often display enhanced catalytic performance than their monometallic counterparts because of a synergistic effect.[1] Heterogeneous bimetallic nanoparticles (NPs) consisting of two distinct metals, such as Au–Pt, Au–Cu, Au–Ag and Au–Pd, NPs,[2-7] have attracted considerable attention due to their unique optical, electrical, and catalytic properties compared to the monometallic counterparts.[8,9] Bimetallic nanoparticle systems, in particular, draw higher attention due to their technological and scientific features for improving catalytic properties.[10] As is well known, for conventional heterogeneous catalysis, bimetallic catalysts often show tunable and synergistic effects compared to their monometallic counterparts. Moreover, it has been shown that the incorporation of a second metal can also effectively improve the photocatalytic performance of Au-based plasmonic photocatalysts. Recently, various bimetallic nanostructures consisting of noble metals such as Au, Ag, Pd, and Pt have been reported by controlling their composition and morphology.[11-13] Mariscal and co-workers reported the synthesis of Au@Pd core shell nanoalloys and the growth mechanism of Au(core)–Pd(shell) bimetallic NPs.[14] Han et al. demonstrated selective deposition of Au-Pd alloy at the ends of Au nanorods for generation of Au-Pd alloy horns.[15] Most of the bimetallic NPs were used as all kinds of catalysts. In 2011, octapodal Au-Pd alloy NPs synthesized by one pot method and used as an electrocatalyst.[5] And hollow Au@Pd and Au@Pt core–shell NPs reported by Khashab used as electrocatalyst for ethanol oxidation.[2,6] Lakshminarayanan et. al reported Au@Pd core-shell NPs on a graphite rod and used as electrocatalyst in methanol oxidation reaction.[7] Colmenares et al. reported the bimetallic Pd-Au/TiO_2 as photocatalyst to selective oxidation of methanol to methyl formate with highly active.[16] Due to its good catalytic properties, the alloy bimetallic NPs can be explored to use in analysis, such as the Au@Pd core–shell nanostructures have been applicated in the electrochemical analysis for thrombin,[4] and $Pt_{74}Ag_{26}$ NPs decorated ultrathin MoS_2 nanosheets (MoS_2-$Pt_{74}Ag_{26}$) was used as novel peroxidase mimics for highly selective colorimetric detection of H_2O_2 and glucose, which has higher affinity for H_2O_2 with good reusability.[1] Although various bimetallic NPs have been extensively studied for diverse catalysis applications, due to this structural diversity makes it more difficult to achieve controllable synthesis of bimetallic nanomaterials, there remain several challenges to be overcome.

However, due to their high cost and scarcity of the noble metal, there has been an increasing trend toward decrease the usage and reuse of the noble metal nanoparticles. Otherwise, due to their small sizes, large surface areas and without a suitable support, as nanocatalysts, metal NPs could not recycle from reaction solution because they are easily aggregate in solution. To improve the efficiency and save resources, there has been an increasing trend toward the use of magnetically retrievable NPs in efficient green chemical synthesis. Magnetic NPs, such as Fe_3O_4, are particularly useful support materials for catalysts as they can combine the advantages of high dispersion through a liquid with ease of recovery. It can not only prevent the aggregation of bimetallic nanoparticles, but also facilitate the recycle of nanocatalysts through magnetic separation.[17,18] The activity of bimetallic NPs can be further enhanced by making porous hollow structures.[19,20] Continuous efforts have been made towards the development of such materials in order to achieve the desired properties and activities.

Key Laboratory of Design and Synthesis of Functional Materials and Green Catalysis, Colleges of Heilongjiang Province, College of Chemistry and Chemical Engineering, Harbin Normal University, 150025, P. R. China E-mail: fangchai@gmail.com, jiangjingjie80@163.com, qufengyu@hrbnu.edu.cn

Electronic Supplementary Information (ESI) available: [TEM, SEM and catalytic data]. See DOI: 10.1039/x0xx00000x

Here, we synthesized magnetic bimetallic Fe_3O_4@Au-Pd hybrid NPs by using the Fe_3O_4 hollow spheres as templates. It was found that the as-prepared Fe_3O_4@Pd and Fe_3O_4@Au-Pd hybrid NPs exhibit high activity as catalysts for the reduction of 4-nitrophenol (4-NP) and potassium hexacyanoferrate (III) ($K_3Fe(CN)_6$) by $NaBH_4$. Using an external magnetic field, the magnetic Pd and bimetallic catalysts can be easily recycled in next reaction and exhibit high reusability. Thus, the present article intends to highlight the development of bimetallic magnetic porous structured Au-Pd NPs and to study their reactivity towards catalytic 4-NP and Potassium hexacyanoferrate (III) reduction. The catalysis for reduction of other nitrophenols including 2-nitrophenol, 3-nitrophenol and 4-nitrothiophenol were also investigated.

Experimental section

Chemicals

All chemicals used were of analytical grade or of the highest purity available. Ferric chloride hexahydrate ($FeCl_3 \cdot 6H_2O$), sodium acetate anhydrous (NaAc), trisodium citrate ($C_6H_5O_7Na_3 \cdot 2H_2O$) were obtained from Fengchuan Chemical Company (Tianjin, China). Polyethylene glycol 2000 (PEG-2000) was purchased from Tianjin Guangfu Technology Development Co., Ltd. (Tianjin, China). Ethylence glycol (EG), ethanolamine (ETA) and ethanol was provided by Sinopharm Chemical Reagent Co., Ltd (Shanghai, China). Hydrogen tetrachloroaurate (III) trihydrate ($HAuCl_4 \cdot 3H_2O$, 99.9%), palladium chloride ($PdCl_2$, 99%), 3-aminopropyl-triethoxysilane (APTES), 3-nitrophenol (3-NP), 4-nitrothiophenol (4-NTP) and sodium borohydride ($NaBH_4$, 98%) were obtained from Aladin and used as received. Potassium hexacyanoferrate (III) ($K_3Fe(CN)_6$, 99%), 2-nitrophenol (2-NP) and 4-nitrophenol (4-NP) were supplied by Shanghai Chemical Corp. All glassware was thoroughly cleaned with freshly prepared 3:1 HCl/HNO_3 (aqua regia) and rinsed thoroughly with Mill-Q (18.2 MΩ cm^{-1} resistance) water prior to use.

Characterization

The morphology and size and of the materials were characterized by transmission electron microscope (TEM), high resolution TEM (HRTEM) and high angle annular dark-field scanning TEM (HAADF-STEM) imaging and elemental mappings were examined on a JEM-2010 (Japan) operated at 200 kV. Scanning electron microscopy (SEM) image and energy-dispersive X-ray spectroscopy (EDS) analysis were obtained by using a Hitachi Su-70 electron at a celeration voltage of 20 KV. The X-ray photoelectron spectroscopy (XPS) was recorded on an Axis Ultra DLD (SHIMADZU, Japan), and the C1s line at 284.6 eV was used as the binding energy reference. X-ray powder diffraction (XRD) pattern was carried out by using a Rigaku DMax-2600 PC diffraction meter using monochromatic Cu Ka radiation. Magnetic properties of the samples were measured vibrating sample magnetometer (VSM, Lake-shore 7410) at room temperature. Absorption spectra were recorded on a UV–vis spectroscopy was performed with a UV-2550 spectrophotometer (SHIMADZU, Japan) at room temperature. The Au and Pd content in the materials were estimated with an Optima 5300DV Inductively Coupled Plasma Optical Emission Spectrometer (ICP-OES) spectroscopy.

Preparation of Fe_3O_4 hollow spheres

Firstly, the monodisperse Fe_3O_4 hollow spheres were prepared in accordance with the reported literature with slight modifications.[21,22] In detail, 1.05 g of $FeCl_3 \cdot 6H_2O$ was dissolved in 28 mL of mixed solvent containing EG (21 mL) and ETA (7 mL) to form a orange solution. Then, 2.8 g of NaAc and 0.7 g PEG-2000 were added into above solution under vigorously stirring until completely dissolved. Then the above solution was transferred to a Teflon-lined stainless-steel autoclave, sealed and heated at 200°C for 8 h. When the autoclave was cooled to ambient temperature naturally, the black products were collected by a permanent magnet, after washed with water and ethanol for several times. The Fe_3O_4 hollow spheres were obtained by drying at 60 °C for 12 h.

Synthesis of Fe_3O_4@Pd hybrid nanoparticles (Fe_3O_4@Pd NPs)

To adhere the resultant metal NPs strictly, the surface of Fe_3O_4 hollow spheres was modified by APTES. According to previous method,[23] the dispersion solution of Fe_3O_4 hollow nanospheres was dispersed into an ethanol solution of APTES, and then the suspension was continuous mechanical stirred 3 h at room temperature. Finally, the APTES-modified Fe_3O_4 hollow nanospheres were collected and washed with deionized water and ethanol with the help of a magnet, and redispersed in water to form a homogeneous dispersion. Then, 25 mL of above APTES-Fe_3O_4 suspension was added into 200 μL of 112 mM $PdCl_2$ solution, the mixture was mechanically stirred for 2 h, then a given volume of fresh aqueous $NaBH_4$ (10 mM) was added into the above mixture with continuous mechanical stirring 3 h at room temperature. Finally, the Fe_3O_4@Pd hybrid NPs were formed and separated by a magnet. After washed with deionized water and dried in vacuum at 50℃ for 6 h, the Fe_3O_4@Pd hybrid NPs were obtained. It is notable that the rest solution is colorless after separated, suggesting that nearly all the $PdCl_2$ was reduced and generated to Pd NPs, which were all immobilized into the catalyst carriers.

Synthesis of Fe_3O_4@Au nanoseeds and Fe_3O_4@Au-Pd NPs

To synthesize the bimetallic Fe_3O_4@Au-Pd hybrid NPs, the gold nanoseeds were prepared and adhered on the Fe_3O_4 hollow spheres first. The 3.5 nm gold NPs were used as nanoseeds, which were prepared by using the $NaBH_4$ as reduction.[24] To prepare the Fe_3O_4@Au nanoseeds, a 15 mL of the Au nanoseeds solution was mixed with 25 mL of aqueous dispersion of APTES modified Fe_3O_4 hollow spheres by quick ultrasonication. The above mixture was stirring for 2 h, and the Fe_3O_4@Au nanoseeds were collected with a magnet. After washed with ethanol and deionized water 3 times, the Fe_3O_4@Au nanoseeds were redispersed in water to form a homogeneous dispersion for preparing the Fe_3O_4@Au-Pd hybrid NPs. A 25 mL of Fe_3O_4@Au nanoseeds suspension was mixed with an aqueous $PdCl_2$ solution (100 μL, 112 mM), the mixture was mechanically stirred in a closed round bottom flask for 2 h. After a fresh aqueous $NaBH_4$ (10 mM) was added into the above mixture, the Pd NPs were reduced and the Fe_3O_4@Au-Pd NPs were prepared. The mixture was continuous mechanical stirred 3 h at room temperature. After separated using a magnet, washed with deionized water and ethanol, and dried in vacuum at 50℃ for 6 h, the Fe_3O_4@Au-Pd NPs were obtained.

Catalytic reduction of 4-nitrophenol (4-NP)

The catalytic properties of Fe_3O_4@Pd and Fe_3O_4@Au-Pd NPs were systematically examined according to the previous method.[25] For

catalytic reduction of 4-NP, aqueous solutions of 4-NP (0.01 M, 0.03 mL) and freshly prepared aqueous $NaBH_4$ solution (0.5 M, 0.2 mL) were mixed with water (2.5 mL) in a quartz cuvette without stirring. Then the Fe_3O_4@Pd or Fe_3O_4@Au-Pd NPs aqueous suspension (25 μL, 2.8 mg·mL^{-1}) was injected as catalyst without any stirring and ultrasonication. The reaction was monitored by taking absorption spectra. The reusability was investigated by separating the used catalysts were from the solution with a magnet for next cycle of catalytic reaction, after the reduction process was complete. To ensure the quantity of catalyst was enough to reuse in the process of recycle, the 100 μL, 2.8 mg·mL^{-1} of catalyst was added in reaction solution.

Catalytic reduction of $K_3Fe(CN)_6$.

The reduction of $K_3Fe(CN)_6$ was also investigated and monitored using Fe_3O_4@Pd or Fe_3O_4@Au-Pd NPs as catalysts.[25,26] The reduction of $K_3Fe(CN)_6$ was carried out according to a typical reaction,[26] 0.4 mL of 8×10^{-3} M $K_3Fe(CN)_6$ was added in 1.2 mL deionized water, then a 25 μL of suspension of catalyst was added, followed by the rapid addition of 0.8 mL of 0.040 M fresh $NaBH_4$ solution. The process of recycle was similar to the above experiments.

Result and conclusion

As illustrated in scheme 1, the process of preparition of the catalyst and catalysis was depicted clearly. The two kind of recycled catalysts, Fe_3O_4@Pd and Fe_3O_4@Au-Pd, have been synthesized by using the Fe_3O_4 hollow spheres as template. Briefly, Fe_3O_4 hollow spheres were firstly synthesized by using a modified solvothermal method.[21,22] The Fe_3O_4@Pd hybrid NPs were prepared by reducting the $PdCl_2$ to Pd NPs on the surface of Fe_3O_4 hollow spheres. And the Fe_3O_4@Au-Pd hybrid NPs were generated in the form of the seeded growth in situ by Pd^{2+} was directly reduced on the surface of Fe_3O_4@Au nanoseeds. When Fe_3O_4@Au nanoseeds are added into $PdCl_2$ (II) solutions (baths), Pd(II) reduction is catalyzed and leads to palladium deposition on the surface of Au seeds, yielding Au@Pd NPs. Since the reduction of Pd^{2+} ions could only occur on the surface of Au seeds due to the Au catalysis, the newly formed Pd atoms would nucleate and grow on the same, leading to the formation of core–shell Au–Pd NPs.[27] The Pd and bimetallic Au-Pd NPs were fixed and inlayed on the outer surface of the Fe_3O_4 spheres act as robust antenna, which could augment the contact area with reactants. And the Fe_3O_4@Pd and Fe_3O_4@Au-Pd can be reused as catalysts in the next cycle by a magnet. The catalytic activity of two catalysts was compared in the reduction of 4-NP and $K_3Fe(CN)_6$ (III) by $NaBH_4$ in water.

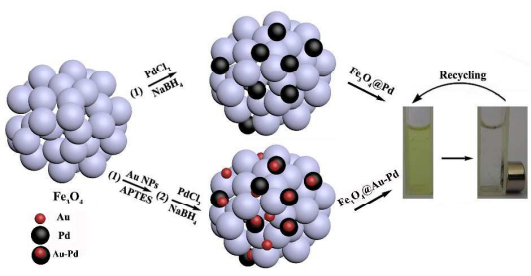

Scheme 1 View of the preparation process and the evaluation of catalysis activity Fe_3O_4@Pd and Fe_3O_4@Au-Pd hybrid NPs.

The crystalline and phase of Fe_3O_4@Pd and Fe_3O_4@Au-Pd hybrid NPs can be inferred by XRD. The Fig. 1 shows diffraction signals of Fe_3O_4, Fe_3O_4@Pd and Fe_3O_4@Au-Pd NPs in XRD analysis. The sharp diffraction peaks (Fig. 1a) were indexed to (112), (211), (202), (220), (312), (303), (224), (332), (143) and (404) Bragg reflection of crystalline cubic inverse spinel of bulk Fe_3O_4 (JCPDS no. 75-1609).[21] Except the characteristic diffraction peaks of Fe_3O_4, the Fig. 1b also took on the (111), (200), (220) and (311), attribute to Bragg reflection of crystalline of Pd (JCPDS no. 05-0681),[28] which proved characteristic diffraction patterns of the fcc lattice planes of metallic Pd (0) were observed for Fe_3O_4@Pd. The addition of Au and Pd metal precursors during the synthesis does not significantly alter the crystallinity of the Fe_3O_4 hollow spheres (Fig. 1c). Notably, no reflections assignable to metallic Au was present in the XRD patterns of Fe_3O_4@Au-Pd NPs, which is possibly due to the low content and high dispersity of the added Au (Fig. 1c). But the existence of Au in the Fe_3O_4@Au-Pd NPs can be proved by the ICP and EDS measurement.

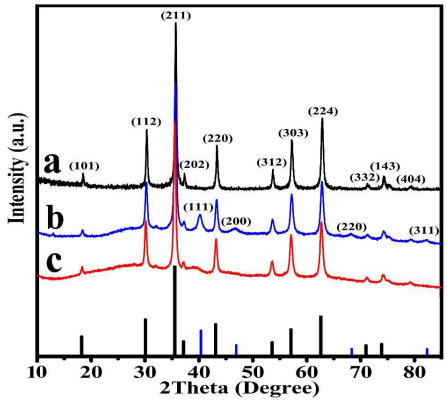

Fig. 1 XRD patterns of (a) Fe_3O_4 hollow spheres, (b) Fe_3O_4@Pd, (c) Fe_3O_4@Au-Pd NPs, and the corresponding standard cards (Fe_3O_4: black and Pd: blue).

The morphology, size distribution and component of the Fe_3O_4@Pd and Fe_3O_4@Au-Pd NPs were detected by TEM measurements. As illustrated in Fig. 2a, the diameter of the Fe_3O_4 hollow spheres was about 100±10 nm. The Fe_3O_4 hollow spheres were performed by many basic Fe_3O_4 NPs with diameter about 25±5 nm. Based the Fe_3O_4 hollow spheres, the hollow hole of Fe_3O_4@Pd NPs can be observed in Fig. 2b, and the diameter of Pd NPs was about 20 nm. The small dimensions of the Pd NPs are further confirmed by the HRTEM image in Fig. 2c. As can be seen, the HRTEM image displays the crystalline lattice structure inside the Pd NPs. The lattice planes of the Pd NPs exhibited no stacking faults or twins, indicating a single-crystalline nature, and the lattice fringe spacing was measured to be 0.202 nm, which is in accordance with Pd (200) planes. The EDS of the Fe_3O_4@Pd hybrid NPs was provided in the Fig. S1, which proved the existence of Pd element, and was in accordance with the XRD data.

A TEM image of the individual Au nanoseed was shown in Fig. S2, which indicated the little nanoseeds can be observed on the surface and hollow holes of the Fe_3O_4 spheres. Fig. 2d provided the TEM image of the Fe_3O_4@Au-Pd NPs, and the size distribution can be seen in the Fig. S3, the diameters of Au NPs were about 3.5 nm, and Au@Pd NPs were about 20-25 nm, respectively.

From the image, the noble NPs can be detected distributed uniformly. The HRTEM was used to confirm the Au and Pd NPs definitely. The HRTEM images displayed the crystalline lattice structure inside the Au and Pd NPs in Fig. 2e, respectively. The HRTEM image also revealed the continuous lattice fringes from the Au core to the Pd shell, indicating an epitaxial relationship between these two metals. The lattice fringe spacing was measured to be 0.205 nm (Fig. 2e), which is in accordance with Au (200) planes. And the lattice fringe spacing was measured to be 0.237 nm (Fig. 2e), which can be attribute to Pd (111) planes.[16,29] As visible from Fig. 2e, our synthesis method resulted in a selected deposition of the external Pd layer at the surface of the Au nanoseeds. The size of the core, which consists in the Au nanoseeds, varies between 3 and 5 nm, whereas the external Au@Pd particles varies in diameter between 20 and 25 nm. Fig. 2f shows the Au@Pd core–shell nanoparticle in the HAADF-STEM image. The distribution of Au and Pd was studied by EDS. Fig. 2f illustrates the EDS line profile of Au and Pd, measured through the center of an individual nanoparticle (marked by a red line in Fig. 2f). As expected, HAADF-STEM image (Fig. 2f) shows the interconnected nanoparticles with two elements of Pd and Au in NPs, both the Au and the Pd signals were clearly traced across the entire particle, which can be illustrated by the EDS elemental line scanning profiles (Fig. 2g). The TEM results strongly demonstrate the formation of Au-Pd bimetallic NPs. The EDS pattern (Fig. 2h) of the Fe_3O_4@Au-Pd NPs confirmed the successful deposition of Au and Pd on the surface of Fe_3O_4 hollow spheres, which was consistant with the ICP results.[14,30-32] The atomic ratio of the Pd: Au was calculated according to ICP analysis was 3.25:1 (Pd: 2.43 wt% and Au: 1.38 wt%).

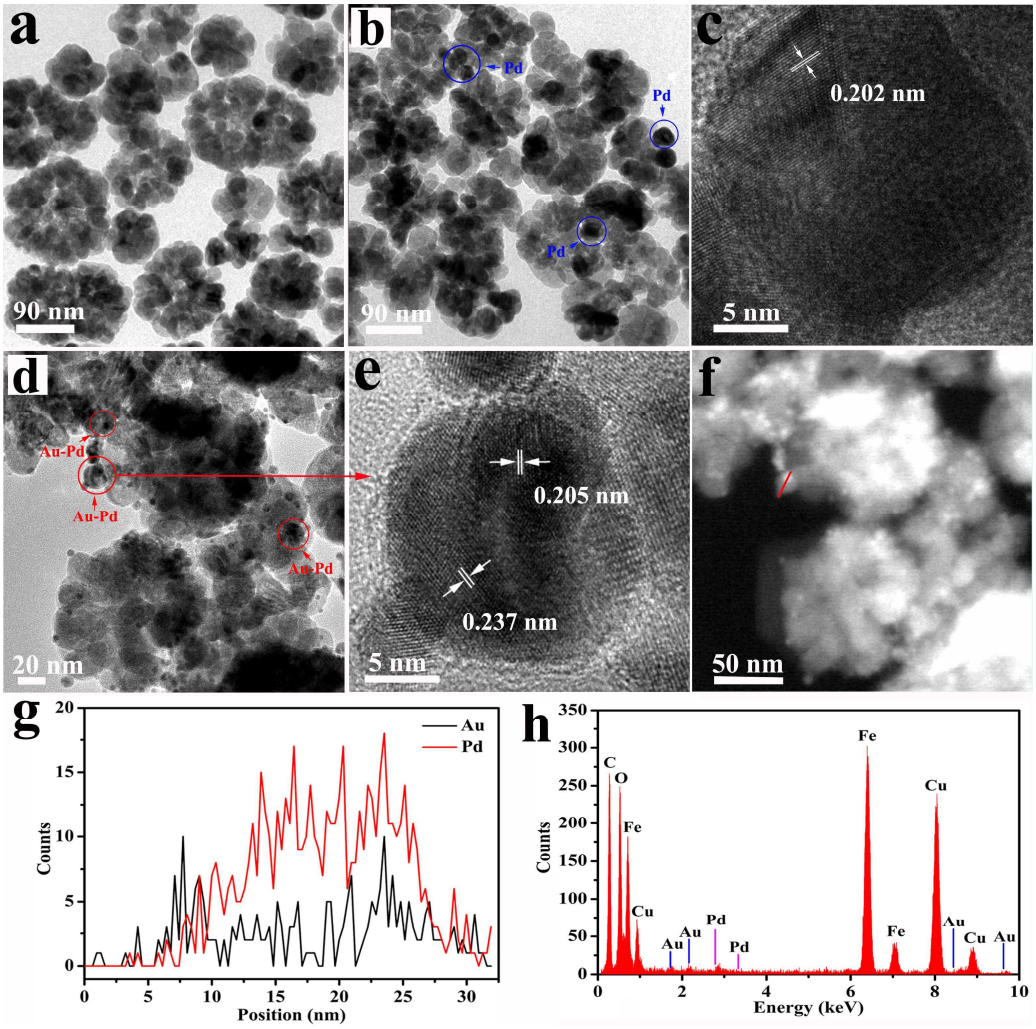

Fig. 2 TEM images of (a) Fe_3O_4, (b) Fe_3O_4@Pd, (c) HRTEM image of Pd NPs, (d) TEM images of Fe_3O_4@Au-Pd NPs, (e) HRTEM image of Au-Pd NPs, (f) HAADF-STEM image of (d), (g) EDS spectrum line profile analysis of a typical Au-Pd NP indicated by the red line in (f), the information of the elemental composition and distribution of the NP, and (h) EDS spectrum of Fe_3O_4@Au-Pd NPs.

The SEM and EDS of the nanocomposites were measured to confirm the morphology, size distribution and hollow structure in detail further. Consistent with the TEM results, the typical SEM images of Fe_3O_4 hollow spheres, Fe_3O_4@Pd and Fe_3O_4@Au-Pd

hybrid NPs (Fig. S4) showed rough surfaces. Fe_3O_4 hollow spheres were uniform and non-aggregated nature with a mean diameter of ~100 nm, which were composed of lots of 25–30 nm small primary Fe_3O_4 NPs. The Pd NPs can be detected in the Fig. 3a, the diameter of Pd NPs was about 20 nm, which was in accordance with TEM. The corresponding EDS was displayed the existence of Pd, Fe and O (Fig. 3b), and other signals in the EDS spectrum arise from silicon slice. The amount of Pd NPs in the Fe_3O_4@Pd NPs was 0.7%. The SEM of Fe_3O_4@Au-Pd NPs indicated that the Au and Pd NPs dispersed on the surface and hole of the Fe_3O_4 hollow spheres (Fig. 3c). The corresponding EDS indicated the existence of Au, Pd, Fe and O (Fig. 3d). Prompted by their porous hollow structure, the nanocomposites should have a higher surface area. Indeed, the Brunauer Emmett–Teller (BET) surface area of Fe_3O_4 hollow spheres, Fe_3O_4@Pd and Fe_3O_4@Au-Pd hybrid NPs (Fig. S5) were 41.71 $m^2 \cdot g^{-1}$, 71.72 $m^2 \cdot g^{-1}$ and 60.87 $m^2 \cdot g^{-1}$, respectively.

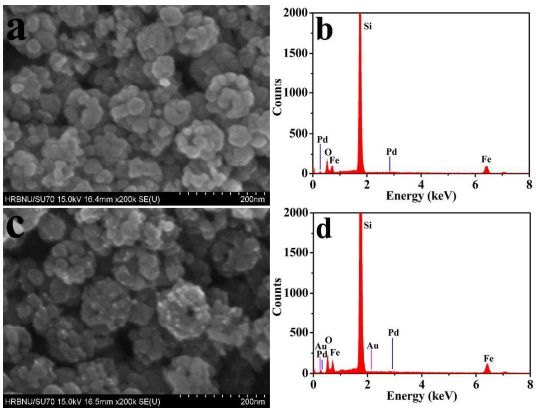

Fig. 3 SEM images of (a) Fe_3O_4@Pd and (c) Fe_3O_4@Au-Pd NPs; EDS spectrum analysis of (b) Fe_3O_4@Pd and (d) Fe_3O_4@Au-Pd NPs.

To evaluate the chemical composition of the hybrid NPs, the XPS analysis on the Au and Pd was carry out (Fig. 4). The XPS survey spectrum of Fe_3O_4@Au-Pd NPs showed peaks due to C_{1s} (284.4 eV), O_{1s} (532.6 eV), Au_{4f} (83.5 eV), and Pd_{3d} (335.2 eV). The Au4f high resolution spectra displayed two peaks can be assigned to $4f_{7/2}$ and $4f_{5/2}$ doublet at 83.5 and 87.1 eV, respectively (Fig. 4a).[33] The XPS binding energy of Au $4f_{7/2}$ was consistent with zerovalent Au. The high resolution XPS of Pd3d revealed two doublets compared with Au (Fig. 4b). One pair at 335.2 and 341.1 eV corresponding to $Pd_{3d5/2}$ and $Pd_{3d3/2}$, respectively, in good agreement with the literature values (335.5 and 341.1 eV) of bulk Pd(0). The XPS further confirms the formation of the Au-Pd alloys, which is consistent with the previous reports.[34]

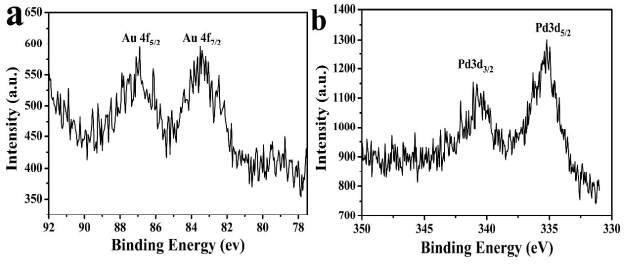

Fig. 4 High-resolution XPS of (a) Au 4f (b) Pd 3d spectrum of Fe_3O_4@Au-Pd NPs.

In order to assess the potential of the nanocomposites in magnetic separation, the magnetic properties of Fe_3O_4@Pd and Fe_3O_4@Au-Pd NPs were characterized by VSM at 300 K, and the magnetic hysteresis loops were illustrated in Fig. 5. These NPs can be easily collected using a permanent magnet, which exhibit characteristic features of superparamagnetism.[35] As depicted in Fig. 5, all of the samples were superparamagnetic and both the remanent magnetizations and coercivities were closed to zero. The magnetization saturation value of the Fe_3O_4 hollow spheres reached 84.93 $emu \cdot g^{-1}$. After coating the Pd NPs, Au-Pd NPs, the magnetization saturation value of Fe_3O_4@Pd and Fe_3O_4@Au-Pd NPs were reduced to 71.93 $emu \cdot g^{-1}$ and 73.79 $emu \cdot g^{-1}$, respectively. The decrease in the magnetization of samples compared with Fe_3O_4 can be attributed to the combined effect of nano-sized Fe_3O_4 particles, robust coating of metal NPs on their surface (quenching of magnetic moment by electron exchange between coating and surface atoms).[36] However, the magnetic saturation value of the samples still remained at a high level, which was large enough to facilitate the quick separation of NPs from solution using a regular magnet (inset of Fig. 5).

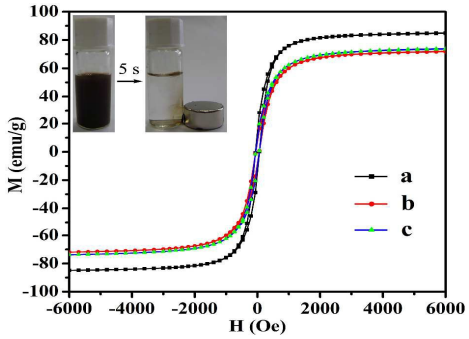

Fig. 5 Magnetization curves of the (a) Fe_3O_4 hollow spheres, (b) Fe_3O_4@Pd, (c) Fe_3O_4@Au-Pd NPs. The insets show their suspensions before and after magnetic separation by an external magnet.

Catalysis

As commonly known, the direct reduction of 4-NP over noble metal particles is considered as a green process for the production of 4-AP.[28,29] 4-NP has caught great public concern due to its causing water pollution, while its derivative, 4-aminophenol (4-AP), is a useful industrial intermediate for antipyretic and analgesic drugs, photographic developers, anticorrosion lubricants.[37, 38] It was of great use that 4-NP could be efficiently reduced to 4-AP. This model reaction has been widely applied to test the catalytic property of noble matal NPs and bimetallic NPs.[39,40] Therefore, the catalytic activity of the Fe_3O_4@Pd and Fe_3O_4@Au-Pd NPs was estimated by the reduction of 4-NP using $NaBH_4$ at 30 °C.

The reaction kinetics could be followed by UV−vis spectroscopy. The aqueous solution of 4-NP shows a maximum absorption at 317 nm, after addition of fresh $NaBH_4$, the absorption red shifted to 400 nm immediately, due to the formation of 4-nitrophenolate anions (Fig. S6). The reduction kinetics could be characterized by the decrease of the absorbance at 400 nm (consumption of 4-nitrophenolate anions) and the appearance of a new absorption peak centered at 300 nm (generation of 4-AP) (Fig. 6a). In order to estimate the efficiency of the catalyst, the

predetermined calibration curve has been confirmed in Fig. S7. According to Wunder,[41] the $NaBH_4$ was present in significant excess in this process, the reduction kinetics of 4-NP can be considered as a pseudo-first-order reaction[42] and a good linear relationship between $\ln(C_t/C_0)$ and reaction time can be obtained.[43] Due to its concentration remained virtually constant during the reaction, the reduction rate was considered to be independent of the $NaBH_4$ concentration. Thus, pseudo-first-order kinetics was used to evaluate the reaction rate of the catalytic reaction.[43] The ratio of C_t to C_0 (C_t/C_0) (where C_t and C_0 are the 4-NP concentrations at time t and time 0, respectively) was measured from the relative intensities of the absorbance at the corresponding times. As expected, a linear relationship between $\ln(C_t/C_0)$ and reaction time was obtained, as shown in inset of Fig. 6. Thus, the rate constants were estimated from the slope of the best-fit line as ca. 14.5 and $28.9\times10^{-3}\cdot s^{-1}$, respectively.[43] In comparison, the Fe_3O_4@Au-Pd NPs have exhibited almost double catalytic activity than mono-component Pd counterparts at the same conditions. The catalytic efficiency of noble metal NPs were critically depend on their size, morphology, chemical composition, and surface structure.[44,45] In particular, bimetallic NPs with designed compositions and morphologies generally show enhanced catalytic activities compared with their monometallic counterparts, owing to the geometric, electronic and synergistic effect between different components.[46,47] The comparison of catalytic activity between this work with some reported catalysts was performed. Remarkably, the value of TOF is much higher than those of the Au-Pd hybrid NPs (Table S1), which confirmed that Fe_3O_4@Au-Pd NPs was a high efficient catalyst.

The binary superiority is attributed to the synergistic effects of Au and Pd. The addition reaction near and at the already present Pd particles allows Au–Pd bimetallic interfaces, the number of which depends on the Au concentration influencing nucleation sites and final size of Au growth.[48] Bimetallic interfaces as well as close proximity (Fig. 2e) of metals with different chemical absorption characteristics and work functions are highly desired in catalysts.[48] And the charge redistribution in the Au-Pd NPs could suppress oxidation of Pd.[49-51] Otherwise, the Pd ensembles could form upon the addition of Au.[49-51] These effects may improve the catalytic performance of the bimetallic hybrid.

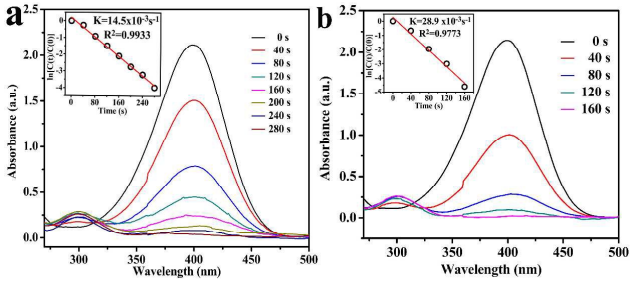

Fig. 6 UV-vis spectra and kinetic rate of the reduction of 4-NP by $NaBH_4$ in the presence of (a) Fe_3O_4@Pd and (b) Fe_3O_4@Au-Pd NPs. Insets: the corresponding $\ln(C_t/C_0)$ versus reaction time for reduction of 4-NP.

Recyclability of catalysts is an important parameter from the industrial point of view to ascertain its long term use, to test the reusability of Fe_3O_4@Pd and Fe_3O_4@Au-Pd NPs, six successive cycles of catalytic reduction was repeated by using same catalyst. The reaction processes were monitored using UV-vis spectroscopy (Fig. S8 and Fig. S9), respectively. The corresponding reduction kinetics (inset of Fig. S8 and Fig. S9) were surveyed, and the reaction rate constant k was determined respectively. According to the UV-vis spectra (Fig. S8), using Fe_3O_4@Pd as catalyst, the kinetic rate of reaction were calculated to $20.51\times10^{-3}\cdot s^{-1}$, $13.71\times10^{-3}\cdot s^{-1}$, $5.58\times10^{-3}\cdot s^{-1}$, $3.99\times10^{-3}\cdot s^{-1}$, $2.55\times10^{-3}\cdot s^{-1}$ and $2.13\times10^{-3}\cdot s^{-1}$, respectively. For comparison, the recyclability of two catalysts was examined at same condition, the Fe_3O_4@Au-Pd NPs exhibited higher catalytic activity which were calculated to $35.31\times10^{-3}\cdot s^{-1}$, $16.46\times10^{-3}\cdot s^{-1}$, $7.57\times10^{-3}\cdot s^{-1}$, $4.03\times10^{-3}\cdot s^{-1}$, $3.44\times10^{-3}\cdot s^{-1}$ and $2.60\times10^{-3}\cdot s^{-1}$ in the 6 successive cycles (Fig. S9). The bimetallic Au-Pd NPs also displayed better catalytic behaviour in comparison to monometallic Pd NPs in recyclability. The decrease in efficiency of the catalyst can be attributed probably to the reduction in the surface active sites of the catalyst. The catalysts were thus found to be stable up to at least 6 runs with conversion efficiency of around 100% (Fig. 7).

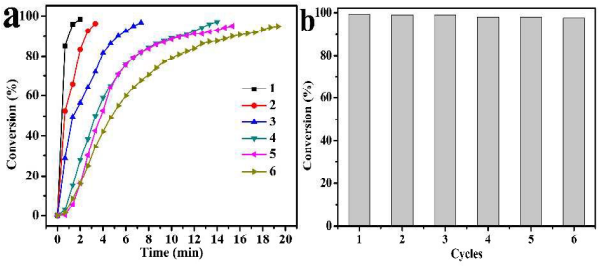

Fig. 7 (a) Relationship of the conversion (%) of 4-NP and the reaction time over Fe_3O_4@Au-Pd NPs catalysts after 1-6 reused, respectively. (b) The reusability of Fe_3O_4@Au-Pd NPs as a catalyst for the reduction of 4-NP with $NaBH_4$.

In order to estimate the stability of catalysts, we investigated the SEM and EDS of the Fe_3O_4@Au-Pd NPs after recycled for different times as a representative. The reacted catalyst recycled 1, 3 and 6 times was recorded by the SEM and EDS, to obtain the information of the morphology and the chemical composition of the catalyst. As can be seen in Fig. S10a, the structure of Fe_3O_4@Au-Pd hybrid NPs was still remained the holonomic sphere with some obvious little Au NPs which were not wrapped up by the Pd NPs on their surface. Compared with the unreacted sample (Fig. 3c), there could not find palpable distinction. The corresponding EDS (Fig. S10b) took on the content of the Au (2.17 wt%), Pd (3.35 wt%) and Fe (74.56 wt%), respectively. When the Fe_3O_4@Au-Pd hybrid NPs recycled 3 times (Fig. S10c), the Au NPs can be not seen from the surface of the spheres, and some of the spheres of the Fe_3O_4@Au-Pd hybrid NPs became dispersed due to the wastage in reaction. After the catalyst were recycled 6 times (Fig. S10e), the morphology of the spheres emerged destroy, some of the spheres have been piled up unregularly, and only few sphere still remained the complete structure. However, the size and morphology of the Au-Pd NPs did not changed all the time. The corresponding EDS (Fig. S10f) stated that all elements were still existed with the content of the Au (1.13 wt%), Pd (3.08 wt%) and Fe (79.83 wt%), respectively, though some of the template of hollow sphere was collapsed. The stability of the catalyst was proved fine, and the catalytic activity reduced gradually at the last 6 recycles. So, the

above results indicated that the Fe_3O_4@Au-Pd hybrid NPs show good stability and reusability.

In addition, the reduction of $K_3Fe(CN)_6$ by $NaBH_4$ was chosen as a model electron-transfer inorganic reaction to evaluate the catalytic efficiency of Fe_3O_4@Pd and Fe_3O_4@Au-Pd NPs and monitored using UV-vis spectroscopy at room temperature. The max absorption peak of light yellow aqueous $K_3[Fe(CN)_6]$ solution was at 420 nm. The intensity of absorption can decrease gradually due to the formation of $K_4[Fe(CN)_6]$ within 12 h after the addition of $NaBH_4$ (Fig. S11). However, after the addition of catalyst, the absorption peak at 420 nm significantly decreased as the reaction procced, and the reaction process totally completed within 150 s and 90 s, respectively. The investigations of UV-vis monitoring demonstrate that the catalytic activity of Fe_3O_4@Au-Pd NPs was better than that of the Fe_3O_4@Pd NPs as catalyst (Fig. 8). Since $NaBH_4$ was present in great excess in the reduction system, the reaction rate was almost independent of its concentration. Thus the reaction kinetics can be evaluated by a pseudo-first-order process with respect to the concentration of $[Fe(CN)_6]^{3-}$. Typical plots of $\ln(C_t/C_0)$ against the reaction time (t) for different catalysts were shown in inset of Fig. 8, where C_t and C_0 are the $[Fe(CN)_6]^{3-}$ concentrations at time t and 0, respectively. The reaction rate constant k was $22.50\times10^{-3}\cdot s^{-1}$ and $36.06\times10^{-3}\cdot s^{-1}$ respectively, which was calculated from the slope of the linear section of the plots of $\ln(C_t/C_0)$ versus t (inset of Fig. 8a and 8b). The results indicated the higher catalytic activity of Fe_3O_4@Au-Pd NPs than Fe_3O_4@Pd NPs toward the reduction of $[Fe(CN)_6]^{3-}$ to $[Fe(CN)_6]^{4-}$ ions.

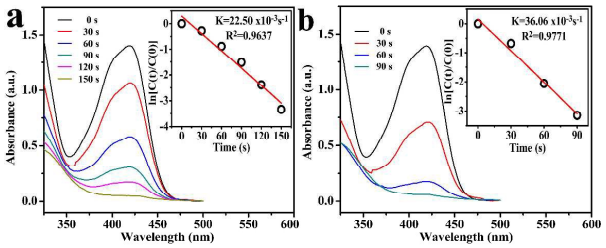

Fig. 8 UV-vis spectra and kinetic rate of the reduction of $K_3Fe(CN)_6$ by $NaBH_4$ in the presence of (a) Fe_3O_4@Pd and (b) Fe_3O_4@Au-Pd NPs. Insets: the corresponding $\ln(C_t/C_0)$ versus reaction time for reduction of $K_3Fe(CN)_6$.

To test the reusability in reduction of $K_3Fe(CN)_6$, 9 successive cycles of catalytic reduction were carried out, respectively. The catalysts can be reused in the process of the recycles, but the effect of the recovered catalyst on the reaction time of subsequent reaction is depressed to 1350 and 690 s gradually after 9 cycles, respectively (Fig. 9, Fig. S12 and S13). As expected, linear correlation of $\ln(C_t/C_0)$ versus t of the all runs were obtained and indicated in the Fig. 9, Fig. S12 and S13. In comparison, the rate constant k of reaction with Fe_3O_4@Pd NPs as catalyst was $29.57\times10^{-3}\cdot s^{-1}$, which was much lower than that of Fe_3O_4@Au-Pd NPs, $40.79\times10^{-3}\cdot s^{-1}$. The same order of catalytic activity, Fe_3O_4@Au-Pd>Fe_3O_4@Pd NPs, was observed in the two kinds of reaction.

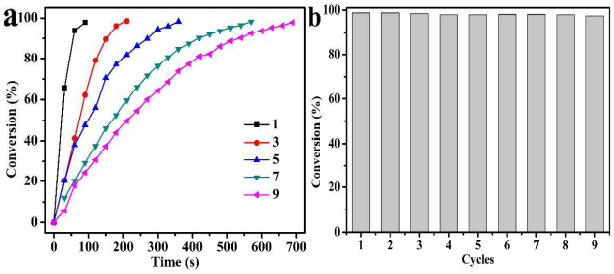

Fig. 9 (a) Relationship of the conversion (%) of $K_3Fe(CN)_6$ and the reaction time over Fe_3O_4@Au-Pd NPs catalysts after 1, 3, 5, 7, 9 reused, respectively. (b) The reusability of Fe_3O_4@Au-Pd NPs as a catalyst for the reduction of $K_3Fe(CN)_6$ with $NaBH_4$.

The catalytic activity of the Fe_3O_4@Au-Pd NPs was also investigated by reduction of other nitrophenols including 2-nitrophenol (2-NP), 3-nitrophenol (3-NP) and 4-nitrothiophenol (4-NTP). The reactions were monitoring by the UV-vis spectra and showed in the supporting information (Fig. S14-S16). The nitrophenols (2-NP, 3-NP) can be degraded by $NaBH_4$ with the Fe_3O_4@Au-Pd hybrid NPs as catalyst within 2 min, and the 4-NTP can be reduced completely in 22 min. The corresponding images showed that the nitrophenols (2-NP, 3-NP and 4-NTP) can be reduced from yellow to colorless (inset of Fig. S14-16). Above experiments proved that the Fe_3O_4@Au-Pd hybrid NPs can be used as catalyst to reduce other nitrophenols except the 4-NP with good catalytic activity. Thus, the above results imply that the Fe_3O_4@Au-Pd NPs act as an excellent recyclable and efficient catalyst towards the reduction of nitrophenols and $K_3Fe(CN)_6$.

Conclusion

In summary, we have demonstrated a facile and efficient route for synthesizing Pd, and Au-Pd alloy NPs on Fe_3O_4 hollow spheres. The magnetic Au-Pd bimetallic hybrid NPs reported herein, which combined Au doping in Pd NPs led to a higher catalytic efficiency. The reproducibility and stability of Fe_3O_4@Pd and Fe_3O_4@Au-Pd NPs were further confirmed. Excellent catalytic activities towards the reduction of nitrophenols and $K_3Fe(CN)_6$ were observed with the prepared, demonstrated the high catalytic activity and satisfying stability. Following this approach, the promising magnetic bimetallic hybrid composites would realize the conversion of nitro to amino compounds on a large scale and would have potential applications in environmental control.

Acknowledgements

The authors gratefully acknowledge the financial support from the NSF of China (Project No. 21205024), the National Hi-Technology Research and Development Program (863 Program) (2013AA032204), the National Science Foundation for Post-doctoral Scientists of China (Grant No. 2012M520659, 2013T60307), the Natural Science Foundation of Heilongjiang Province (B201305), the project of Harbin Science and Technology bureau (2014RFQXJ151).

Notes and references

1 S. F. Cai, Q. S. Han, C. Qi, Z. Lian, X. H. Jia, R. Yang and C. Wang, *Nanoscale*, 2016, **8**, 3685–3693.

2 H. M. Song, D. H. Anjum, R. Sougrat, M. N. Hedhili and N. M. Khashab, *J. Mater. Chem.*, 2012, **22**, 25003–25010.
3 C. Buchner, L. Lichtenstein, S. Stuckenholz, M. Heyde, F. Ringleb, M. Sterrer, W. E. Kaden, L. Giordano, G. Pacchioni and H. J. Freund, *J. Phys. Chem. C*, 2014, **118**, 20959–20969.
4 W. J. Xu, H. Y. Yi, Y. L. Yuan, P. Jing, Y. Q. Chai, R. Yuan and G. S. Wilson, *Biosensors and Bioelectronics*, 2015, **64**, 423–428.
5 J. W. Hong, Y. W. Lee, M. J. Kim, S. W. Kang and S. W. Han, *Chem. Commun.*, 2011, **47**, 2553–2555.
6 H. M. Song, B. A. Moosa and N. M. Khashab, *J. Mater. Chem.*, 2012, **22**, 15953–15959.
7 A. Renjith and V. Lakshminarayanan, *J. Mater. Chem. A*, 2015, **3**, 3019–3028.
8 D. S. Wang and Y. D. Li, *Adv. Mater.*, 2011, **23**, 1044–1060.
9 M. R. Jones, K. D. Osberg, R. J. Macfarlane, M. R. Langille and C. A. Mirkin, *Chem. Rev.*, 2011, **111**, 3736–3827.
10 M. Sankar, N. Dimitratos, P. J. Miedziak, P. P. Wells, C. J. Kiely and G. J. Hutchings, *Chem. Soc. Rev.*, 2012, **41**, 8099–8139.
11 S. J. Guo, S. Zhang, D. Su and S. H. Sun, *J. Am. Chem. Soc.*, 2013, **135**, 13879–13884.
12 G. T. Fu, B. Y. Xia, R. G. Ma, Y. Chen, Y. W. Tang and J. M. Lee, *Nano Energy*, 2015, **12**, 824–832.
13 J. J. Mao, T. Cao, Y. J. Chen, Y. Wu, C. Chen, Q. Peng, D. S. Wang and Y. D. Li, *Chem. Commun.*, 2015, **51**, 15406–15409.
14 A. Spitale, M. A. Perez, S. Mejía-Rosales, M. J. Yacamánd and M. M. Mariscal, *Phys. Chem. Chem. Phys.*, 2015, **17**, 28060–28067.
15 J. F. Huang, Y. H. Zhu, M. Lin, Q. X. Wang, L. Zhao, Y. Yang, K. X. Yao and Y. Han, *J. Am. Chem. Soc.*, 2013, **135**, 8552–8561.
16 J. C. Colmenares, P. Lisowski, D. Łomot, O. Chernyayeva and D. Lisovytskiy, *ChemSusChem*, 2015, **8**, 1676–1685.
17 V. S. Coker, J. A. Bennett, N. D. Telling, T. Henkel, J. M. Charnock, G. Laan, R. A. D. Pattrick, C. I. Pearce, R. S. Cutting, I. J. Shannon, J. Wood, E. Arenholz, I. C. Lyon and J. R. Lloyd, *ACS Nano.*, 2010, **4**, 2577–2584.
18 Y. J. Jiang, G. Z. Li, X. D. Li, S. X. Lu, L. Wang and X. W. Zhang, *J. Mater. Chem. A*, 2014, **2**, 4779–4787.
19 J. Zeng, Q. Zhang, J. Y. Chen and Y. N. Xia, *Nano Lett.*, 2010, **10**, 30–35.
20 H. P. Liang, H. M. Zhang, J. S. Hu, Y. G. Guo, L. J. Wan and C. L. Bai, *Angew. Chem., Int. Ed.*, 2004, **43**, 1540–1543.
21 Y. C. Zhu, J. Lei and Y. Tian, *Dalton Trans.*, 2014, **43**, 7275–7281.
22 H. Deng, X. L. Li, Q. Peng, X. Wang, J. P. Chen and Y. D. Li, *Angew. Chem., Int. Ed.*, 2005, **44**, 2782–2785.
23 X. M. Zhang, S. S. Ye, X. Zhang and L. P. Wu, *J. Mater. Chem. C*, 2015, **3**, 2282–2290.
24 N. R. Jana, L. Gearheart and C. J. Murphy, *Langmuir*, 2011, **17**, 6782–6786.
25 X. J. Sun and D. Qin, *J. Mater. Chem. C*, 2015, **3**, 11833–11841.
26 D. Y. Du, J. S. Qin, T. T. Wang, S. L. Li, Z. M. Su, K. Z. Shao, Y. Q. Lan, X. L. Wang and E. B. Wang, *Chem. Sci.*, 2012, **3**, 705–710.
27 D. Chen, J. Q. Li, P. L. Cui, H. Liu and J. Yang, *J. Mater. Chem. A*, 2016, **4**, 3813–3821.
28 Z. M. Wang, C. L. Xu, G. Q. Gao and X. Li, *RSC Adv.*, 2014, **4**, 13644–13651.
29 J. M. Zheng, Y. L. Dong, W. F. Wang, Y. H. Ma, J. Hu, X. J. Chen and X. G. Chen, *Nanoscale*, 2013, **5**, 4894–4901.
30 W. Zhou, K. Zheng, L. He, R. M. Wang, L. Guo, C. P. Chen, X. D. Han and Z. Zhang, *Nano Lett.*, 2008, **8,** 1147–1152.
31 L. L. He, P. Song, J. J. Feng, W. H. Huang, Q. L. Wang and A. J. Wang, *Electrochimica Acta*, 2015, **176**, 86–95.
32 A. Londono-Calderon, A. Bruma, D. B. Uribe, A. Ponce and M. Jose-Yacaman, *J. Phys. Chem. C,* 2015, **119**, 24621–24626.
33 A. Schejn, T. Mazet, V. Falk, L. Balan, L. Aranda, G. Medjahdi and R. Schneider, *Dalton Trans.*, 2015, **44**, 10136–10140.
34 S. Moussa, V. Abdelsayed and M. S. El-Shall, *Chem. Phys. Lett.*, 2011, **510**, 179–184.
35 G. Q. Liu, D. A. Wang, F. Zhou and W. M. Liu, Small, 2015, **11** 2807–2816.
36 B. Mu and A. Q. Wang, *J. Mater. Chem. A*, 2015, **3**, 281–289
37 K. K. Haldar, S. Kundu and A. Patra, *ACS Appl. Mater. Interfaces,* 2014, **6**, 21946–21953.
38 M. Liang, R. X. Su, R. L. Huang, W. Qi, Y. J. Yu, L. B. Wang and Z. M. He, *ACS Appl. Mater. Interfaces*, 2014, **6**, 4638–4649.
39 Y. Mei, Y. Lu, F. Polzer and M. Ballauff, *Chem. Mater.*, 2007, **19**, 1062–1069.
40 R. Bhandari and M. R. Knecht, *ACS Catal.*, 2011, **1**, 89–98.
41 S. Wunder, F. Polzer, Y. Lu, Y. Mei and M. Ballouff, *J. Phys. Chem. C,* 2010, **114**, 8814–8820.
42 E. E. Finney and R. G. Finke, *Chem. Mater.*, 2009, **21**, 4468–4479.
43 Y. Li, J. Y. Lan, J. J. Liu, J. F. Yu, Z. P. Luo, W. X. Wang and L. Y. Sun, *Ind. Eng. Chem. Res.*, 2015, **54**, 5656–5663.
44 X. Q. Huang, S. H. Tang, H. H. Zhang, Z. Y. Zhou and N. F. Zheng, *J. Am. Chem. Soc.*, 2009, **131**, 13916–13917.
45 Z. Q. Niu, Q. Peng, M. Gong, H. P. Rong and Y. D. Li, *Angew. Chem., Int. Ed.*, 2011, **50**, 6315–6319.
46 B. P. Khanal and E. R. Zubarev, *Angew. Chem., Int. Ed.*, 2009, **48**, 6888–6891.
47 Y. Yan, J. W. Fu, M. H. Wang, S. J. Liu, Q. Q. Xin, Z. M. Chen and Q. Xu, *RSC Adv.*, 2016, **6**, 24921–24928.
48. S. C. Tang, S. Vongehr, G. R. He, L. Chen and X. K. Meng, *J. Colloid. Interf. Sci.*, 2012, **375**, 125–133.
49. C. H. Liu, J. Liu, Y. Y. Zhou, X. L. Cai, Y. Lu, X. Gao and S. D. Wang, *Carbon*, 2015, **94**, 295–300
50. F. Gao and D. W. Goodman, *Chem. Soc. Rev.*, 2012, **41**, 8009–8020.
51. C. H. Liu, R. H. Liu, Q. J. Sun, J. B. Chang, X. Gao, Y. Liu, S. T. Lee, Z. H. Kang and S. D. Wang, *Nanoscale*, 2015, **7**, 6356–6362.

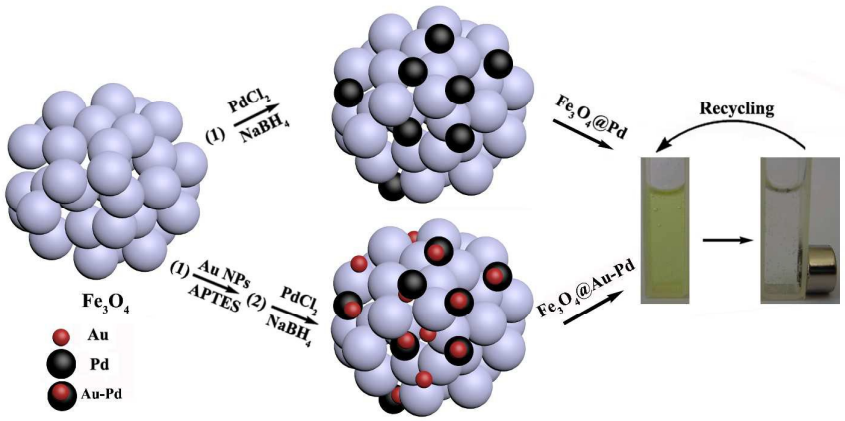

View of the preparation process and the evaluation of catalysis activity Fe_3O_4@Pd and Fe_3O_4@Au-Pd NPs.